Surface Al and Co coordination for peroxymonosulfate activation: Identification and mechanism

Min-Ping Zhu [a,b], Jia-Cheng E. Yang [a,*], Daqin Guan [c], Baoling Yuan [d], Xiaoguang Duan [e], Darren Delai Sun [f,*], Chenghua Sun [g], Shaobin Wang [e], Ming-Lai Fu [a,h,**]

[a] Key Laboratory of Urban Pollutant Conversion, Institute of Urban Environment (IUE), Chinese Academy of Sciences (CAS), No. 1799, Jimei Avenue, Xiamen 361021, China
[b] University of Chinese Academy of Sciences (UCAS), No. 19(A), Yuquan Road, Shijingshan District, Beijing 100049, China
[c] Department of Building and Real Estate, The Hong Kong Polytechnic University, Hung Hom, Kowloon 999077, Hong Kong, China
[d] Key Laboratory of Songliao Aquatic Environment, Ministry of Education, Jilin Jianzhu University, Changchun 130118, China
[e] School of Chemical Engineering and Advanced Materials, The University of Adelaide, Adelaide, SA 5005, Australia
[f] School of Civil and Environmental Engineering, Nanyang Technological University, 639798, Singapore
[g] Faculty of Science, Engineering & Technology, Swinburne University of Technology, Victoria 3122, Australia
[h] Xiamen Key Laboratory of Municipal and Industrial Solid Waste Utilization and Pollution Control, College of Civil Engineering, Huaqiao University, Xiamen 361020, China

ARTICLE INFO

ABSTRACT

Deciphering the metal-support interaction-oriented catalysis on millimeter-scaled catalysts is highly desirable yet remains scarce in Fenton-like catalysis. Herein, we fine-tune the support-surface reconstruction of Co_2AlO_4 on γ-Al_2O_3 millispheres and reveal the origins of its activity in peroxymonosulfate activation by nuclear magnetic resonance and X-ray photoelectron/adsorption spectroscopy. Calcination of γ-Al_2O_3 supports rearranged their surface octahedral, tetrahedral and pentacoordinate Al^{3+}. The reconstructed tetrahedral and pentacoordinate Al^{3+} as binding sites regulated the formation of Co_2AlO_4 with coordinated Co^{3+}/Co^{2+} redox centers via strong metal-support interactions. The activities of tailored Co_2AlO_4 @Al_2O_3 millispheres in activating peroxymonosulfate follow different binomial models, highly relying on their Co^{3+}/Co^{2+} ratio, contents of lattice O and pentacoordinate Al^{3+}. The Co-O-Al bonds endow the millimeter-scaled Co_2AlO_4 @Al_2O_3 with robust catalytic activity, stability and reusability. The exposed Co_2AlO_4 (200) surface is responsible for the decomposition of PMS into produce $SO_4^{\bullet-}$ and $^1O_2$ as the dominant oxidants for water detoxification.

1. Introduction

An advanced oxidation process (AOP) is a promising technique for removing the recalcitrant pollutants in wastewaters [1]. Substantial efforts have been directed to designing and optimizing the metal-based heterogeneous catalysts to obtain on-demand AOP performance [2,3]. Thanks to the unique advantages of metal-organic frameworks (MOFs), such as high surface area, low density, variable pore size/surface and tunable topological structures, MOFs and their derivatives have been widely used in the fields of adsorption and catalysis [4–7]. Currently, constructing one-(1D)/two-dimensional (2D) MOFs-based materials is a research hotspot in heterogeneous AOPs [8–11]. Unfortunately, the

1D/2D MOFs-based catalysts in their powder forms are not suitable for practical applications due to the high mass-transfer resistance within the filter column or the difficulty/complexity of their recycling/reusing. To overcome these engineering bottlenecks, millimeter-scaled supports (such as zeolite beads [12], carbon sponge [13], Al_2O_3 ceramic membrane [14], and γ-Al_2O_3 pellets [15,16]) had been used to fabricate monolithic MOFs-based activators/catalysts for producing radicals and nonradical species. The key benefit of these MOFs-based monoliths in a millimeter scale lies in their highly dispersed catalytic sites and easy recyclability for Fenton-like applications.

Despite significant advances in designing monolithic MOFs-based catalysts, the modulation of MOFs-derived active metal species on

---

millimeter-scaled supports and their catalytic behaviors are not yet fully understood. For example, zeolitic imidazolate framework (ZIF-67) immobilized on Al_2O_3 ceramic membrane can be evolved into a Co_3O_4-based monolithic catalyst via a calcination process [14]. However, our previous work indicates that the in-situ formed ZIF-67 on γ-Al_2O_3 pellets could be directly pyrolyzed into $CoAl_2O_4$ (and/or Co_2AlO_4) composite millispheres [15,16]. We think that the variability of the physico-chemical properties of support surface induced the changeable chemical coordination environment. This can change the binding modes of the nucleation of ZIF-67 on the millimeter-scaled supports, thus leading to variable active metal species/sites. Therefore, large uncertainties occur in quantitatively predicting their catalytic behaviors. Therefore, tailoring and identifying the surface anchoring sites of supports is a prerequisite to precisely modulating the catalytic sites and performance.

Recently, there has been a surge in the studies of the relationships between the surface properties of Al_2O_3-based supports and the formation of supported metal components [17–21]. The structural defects on γ-Al_2O_3 surface are commonly the anchoring sites to immobilize active metal species [22]. Other studies indicate that such "structural defects" are closely related to the coordinatively unsaturated pentacoordinate Al^{3+} (Al_P^{3+}) of γ-Al_2O_3 [23], or the octahedrally coordinated Al^{3+} (Al_{Oh}^{3+}) with an oxygen vacancy [24]. Despite revealing the roles of Al_P^{3+} and

defects in controlling the supported metal catalytic sites [19], it is still challenging to exactly substantiate their roles in regulating MOFs-derived metal sites on the macroscale supports. More evidence implies that the variability of the support surface structures can affect the strong metal-support interactions and change the chemical coordination environment [16]. Till now, little information is available on the comprehensive analysis of the variability of the surface anchoring sites of Al_2O_3 millispheres on the formation of ZIF-67 precursors and their evolution into cobalt aluminate species, not to mention the quantitative property-activity relationships of the geometric/electronic features-tailored macroscale catalysts in Fenton-like reactions.

Herein, we first used a feasible calcination strategy to realize the reconstruction of the surface of Al_2O_3 millispheres (i.e., tailoring the octahedral, tetrahedral and pentacoordinate Al^{3+} sites for the subsequent nucleation of ZIF-67 to form ZIF-67 @Al_2O_3 composites), and then modulated the formation of interfacial Co_2AlO_4 spinel on Al_2O_3 pellets (CAP) and their Fenton-like behaviors. The illustration of constructing millimeter-scaled CAP catalysts is shown in Fig. 1A. The changeable surface Al^{3+} sites of pre-treated Al_2O_3 supports, ZIF-67 @Al_2O_3 precursors and CAPs were traced by solid-state ^{27}Al magic-angle spinning (MAS) nuclear magnetic resonance (NMR) spectroscopy to probe the formation mechanisms of support surface reconstruction-modulated
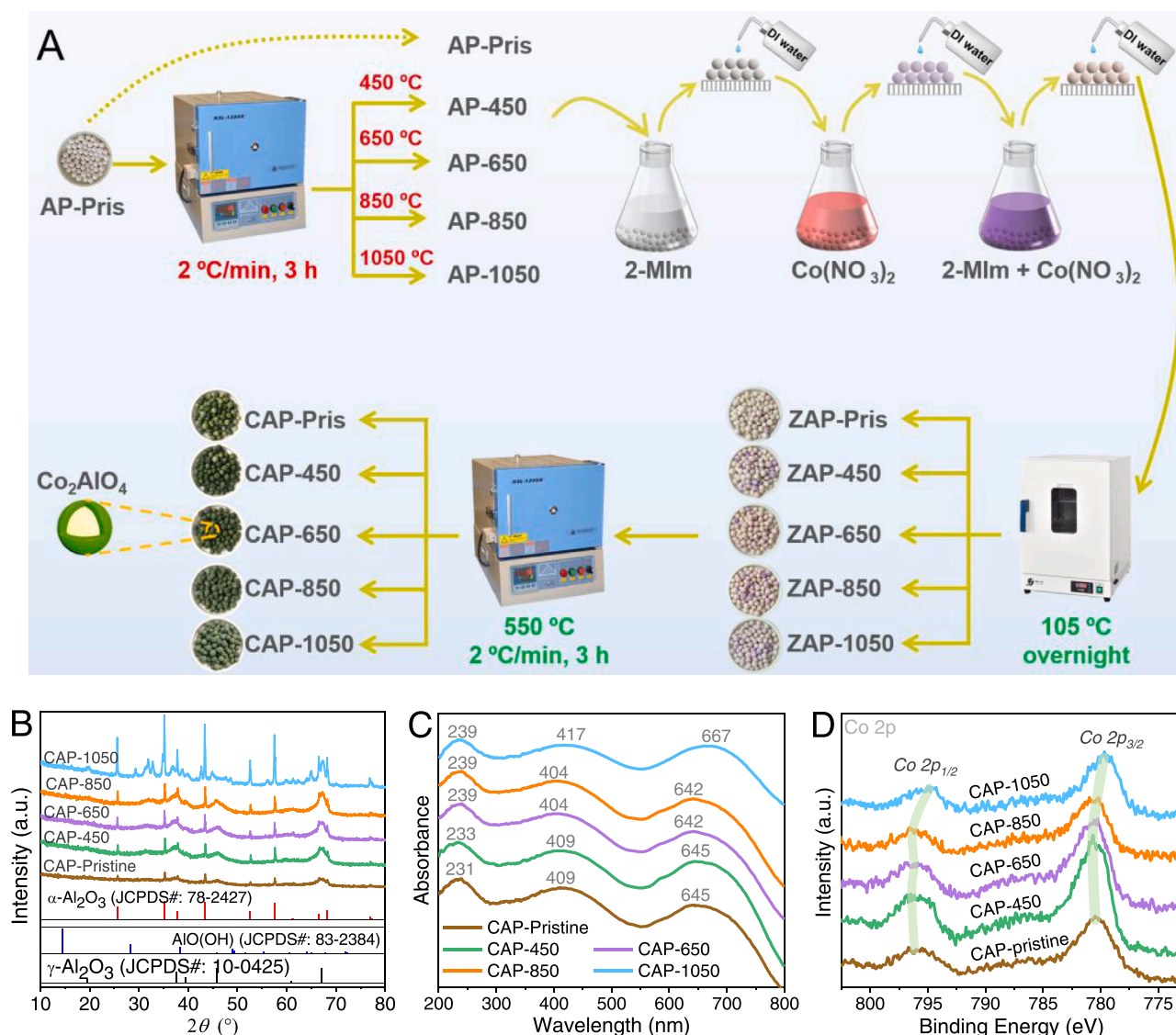

Fig. 1. Illustration for the preparation route of CAP samples (A), and their XRD patterns (B), UV–vis spectra (C) and Co 2p spectra (D).

CAPs, thus establishing the nonlinearly quantitative property-activity relationships for CAPs-mediated peroxymonosulfate (PMS) activation. The analysis of high-resolution transmission electron microscopy (HR-TEM), X-ray photoelectron spectra (XPS), and X-ray absorption spectroscopy (XAS) as well as theoretical calculations were used to reveal the underlying mechanisms in PMS activation. Reported here is a pioneering work of using a simple calcination strategy to modulate the reconstruction of the surface Al_2O_3 millispheres to regulate the formation interfacial Co_2AlO_4 spinel on the Al_2O_3 pellets. This study provides new insights into the modulation of the strong metal-support interactions to develop novel spinel composite millispheres as Fenton-like catalysts via a support surface reconstruction strategy.

2. Experimental section

2.1. Catalysts preparation

The chemicals used in this work are listed in Text S1. Prior to use, commercial γ-Al_2O_3 pellets (APs, with a diameter of 3 – 5 mm) were washed with deionized (DI) water, followed by a drying procedure at 105 °C overnight. The detailed procedures of fabricating millimeter-scaled composite catalysts are shown in Fig. 1A. First, APs were pre-treated via a box furnace under different calcination temperatures (i. e., 450, 650, 850, and 1050 °C) for 3 h in an aerobic environment, and the elevating rate was set as 2 °C/min. The resultant samples were denoted as AP-*x* (*x* = 450, 650, 850, and 1050 °C). Second, the AP-*x* samples were successively immersed into aqueous precursor solutions of ZIF-67 (containing 240 mM 2-methylimidazole and 30 mM Co $(NO_3)_2 \cdot 6 H_2O$) to obtain ZIF-67@Al_2O_3 pellets-*x* (denoted as ZAP-*x*). The detailed immersion procedures are available in Text S2. Last, the ZAP-*x* samples were calcined in static air under 550 °C for 3 h (heating rate of 2 °C/min). After cooling naturally, the dark green Co_2AlO_4 @Al_2O_3 pellets-*x* were obtained (indexed as CAP-*x*). For comparison, APs without calcination (denoted as AP-Pristine) were directly used as the supports to fabricate CAP-Pristine.

2.2. Characterizations

The crystal structures, optical absorption features, morphologies, element valance state and specific surface area of the catalysts were characterized by X-ray diffraction (XRD), UV–vis absorption spectra, HR-TEM, XPS and Brunauer–Emmett–Teller (BET) measurement, respectively. The varied coordination environment of Al atoms in the samples of AP-*x*, ZAP-*x* and CAP-*x* were revealed by the solid-state ^{27}Al MAS NMR. The oxidation state and coordination environment of Co species in fresh CAP-650 were investigated using Co *K*-edge XAS (including X-ray absorption near-edge structure (XANES) and extended X-ray absorption fine structure (EXAFS)). The Co-*L* edge and O-*K* edge XAS spectra of the dried powders of CAP-650 samples before and after activation were used to trace the changes of active centers. Prior to characterization (except for BET measurement), the powder samples should be prepared in advance by directly scraping, colliding or polishing pellet-type samples. The process was carefully operated to collect the active layer from the surface of pellet-type samples. In addition, the actual Co contents within CAP-*x* samples were further analyzed by an inductively coupled plasma optical emission spectrometry (ICP-OES, Optima 7000DV, PerkinElmer, USA) and the mixture of concentrated hydrofluoric acid (HF) and nitric acid (HNO_3) (v/v = 1:1) were used to pretreat the samples before ICP-OES analysis. The details on the above-mentioned characterizations can be found in Text S3.

2.3. Activity tests and theoretical calculations

Using acid orange VII (AO7), carbamazepine (CBZ), bisphenol A (BPA), butylparaben (BPB), 2-chlorophenol (2-CP) and phenol as the model organic pollutants, we examined the catalytic activity, stability

and reusability of CAP-*x* in PMS activation. All the tests were conducted in 100-mL beakers, which were put on a multi-position magnetic stirrer (300 rpm) at room temperature (25 ± 1 °C). In a typical procedure, 80 mL of AO7 solutions (10 mg/L, natural pH = 5.95) and 20 g/L CAP-*x* were added to the beakers. The degradation experiments were then triggered by introducing 0.1 g/L PMS into the above system. At different intervals, an aqueous sample (1 mL) was withdrawn, immediately quenched with ethanol (EtOH, 0.25 mL) and stored in a refrigerator (4 °C). After each test, the optimized CAP-*x* (CAP-650) samples were separated and directly used for the next test to assess their recyclability. Using EtOH (0.1 M and 1.0 M), *tert*-butyl alcohol (TBA, 0.5 M and 5.0 M), and ₗ-histidine (HD, 1 mM) as chemical quenchers, identical procedures were repeated to identify the generation of reactive species (RS) in the CAP-*x*/PMS system and their contributions to the oxidation of organic pollutants. Meanwhile, the RS in the CAP-650/PMS system were further confirmed by electron paramagnetic resonance (EPR) (Bruker ELEXSYS E500). The 5,5-dimethyl-1-pyrroline N-oxide (DMPO) and 2,2,6,6-tetramethyl-4-piperidone (TEMP) were used as the spin trapping reagents with the following operating conditions: Sweep time, 41 s; center field, 3510.35 G; sweep width, 200 G; microwave frequency, 9.85 GHz; microwave power, 20 mW; modulation frequency, 100 kHz; modulation amplitude, 2.0 G. Other reaction conditions for RS detection are: [DMPO] = 100 mM, [TEMP] = 100 mM, [CAP-650] = 0. 25 g/L, [PMS] = 0.2 g/L, pH = 7.0. The residual concentration of AO7 was determined via a UV-Vis spectrophotometer (Evolution 300, Thermo, USA) at 483 nm. The released Co ions were analyzed by an ICP-OES. We also evaluated the applicability of CAP-650 in activating PMS to remove various emerging contaminants (i.e., CBZ, BPA and BPB), chlorinated organic compound (2-CP) and phenol. All the tests were performed in duplicate with their averaged values presented. The detailed procedures and analytical methods for these pollutants can be found in Text S4 and Table S1. The details of DFT calculations for the activation of PMS by CAP-650 can be found in Text S5.

3. Results and discussion

3.1. Characterizations of CAP-x-related materials

3.1.1. Crystal structure

The XRD patterns of CAP-*x*-related samples were studied to trace the change in their crystalline structures. As depicted in Fig. S1A, three broad diffraction peaks (centered at $2\theta = 37.6°, 45.8°$ and $67.0°$) for the pristine AP can be indexed as the (311), (400) and (440) planes of γ-Al_2O_3 (JCPDS#: 10–0425). The other three peaks (centered at $2\theta = 14.5°, 28.2°$, and $72.0°$) could be assigned to the (020), (120) and (200) planes of AlO(OH) (JCPDS#: 83–2384). After calcination (450 – 1050 °C, 3 h), the AlO(OH) phase within pristine AP disappeared while the (012), (104), (113), (024), (116) and (300) planes of α-Al_2O_3 phase appeared (JCPDS#: 78–2427). The intensity of α-Al_2O_3 phase gradually increased as the calcination temperature increased. Other weaker diffractions for AP-1050 are probably due to the poorly crystallized Al_2O_3 phase (between γ- and α-Al_2O_3) [17]. Compared with the AP-*x* sample, the formation/immobilization of Co-related species on the surface of AP-*x* did not alter their XRD patterns except the enhanced intensity (i.e., CAP-*x* sample, Fig. 1B) and the absent peaks for AlO(OH) in CAP-Pristine. Noted that the reflections attributed to the Co-related species were not observed in the XRD patterns. This might be ascribed to the relatively low contents of Co elements (i.e., 0.11, 0.06, 0.07, 0.059 and 0.13 wt% for CAP-Pristine, CAP-450, CAP-650, CAP-850 and CAP-1050, respectively). Another reason is that the signals of the ultrasmall and poorly crystallized Co-related species were below the limits of XRD or covered by the peaks of γ-Al_2O_3 and α-Al_2O_3.

3.1.2. Optical absorption characteristics

As shown in Fig. 1C, three broad bands at 231 – 239, 404 – 417, and 642 – 645 nm are found in the UV–vis spectra of CAP-*x* samples, which

are attributed to the ligand to metal charge transfer (LMCT) process from O_2^{2-} to Co^{3+} in octahedral sites (Co_{Oh}^{3+}) [25], Co^{2+} in octahedral sites (Co_{Oh}^{2+}) [26], and Co^{2+} in tetrahedral coordination (Co_{Td}^{2+}) [25,27], respectively. The band at 667 nm for CAP-1050 can be ascribed to the LMCT process from O^{2-} to Co_{Oh}^{3+} [28]. The above bands indicate the presence of a Co_2AlO_4 phase within CAP-x [27]. The dark green of CAP-x samples stems from their abundant Co_{Oh}^{2+} and Co_{Oh}^{3+} species [25,27]. The varied blue shifts (409 → 404, 645 → 642 nm) or red shifts (231 → 235 → 239, 404 → 417, 642 → 667 nm) for the UV–vis spectra of CAP-x samples probably result from the different spatial coordination ratios of Co^{3+} and Co^{2+} ions [27,29]. The varied spatial coordination states of Co atoms can be confirmed by the XPS Co 2p spectra (Fig. 1D). In detail, the center peaks of Co $2p_{3/2}$ spectra first shifted to higher energy and then changed to lower energy with the continuing increase in the support pre-treatment temperature, which indicates an increase in the proportion of Co^{2+} species first and then that of Co^{3+} species. More information on the evolution of Co^{3+} and Co^{2+} species (based on high-resolution XPS analysis) is provided in Section 3.1.4.

3.1.3. Solid-state ^{27}Al MAS NMR analysis

To better understand how the varied Al^{3+} sites/species regulated the immobilization of Co atoms and the subsequent formation of Co_2AlO_4, we comprehensively studied the solid-state ^{27}Al MAS NMR spectra of AP-x, ZAP-x, and CAP-x samples. As depicted in Fig. 2A – 2E, the NMR spectra of the AP-x supports can be simulated by three peaks at 9.0 – 10.6, 34.1 – 38.8, and 63.2 – 65.5 ppm chemical shifts, which are attributed to the Al^{3+} species in the octahedral (Al_{Oh}^{3+}), pentacoordinate (Al_P^{3+}) and tetrahedral (Al_{Td}^{3+}) coordination, respectively [19,20,30,31]. The calcination of Al_2O_3 supports has resulted in rearrangements of Al_{Oh}^{3+}, Al_P^{3+} and Al_{Td}^{3+} sites. Generally, the Al^{3+} elements within AP-x samples are mainly in their Al_{Oh}^{3+} forms. Interestingly, the ratio of Al_P^{3+} sites gradually decreased from 8.5% to 6.7% with the increase in pre-treatment temperature. Concomitantly, the ratio of the Al_{Oh}^{3+} sites within Al_2O_3 first increased with the raised pre-treated temperature (below 650 °C) and then decreased for those samples calcined above 850 °C. The ratio of Al_{Td}^{3+} sites nearly remained constantly (about 24.5%) until the pre-treated temperature of Al_2O_3 increased to 850 °C. For the Al_2O_3 supports pre-treated below 850 °C, the Al_P^{3+} sites were preferably converted into Al_{Oh}^{3+} ones, while the higher pre-treated temperature (> 850 °C) led to the transformation of Al_P^{3+} sites into Al_{Td}^{3+} sites. This is reasonable because the metal ions occupying the tetrahedral sites can maintain relatively high stability below 800 °C [32].

In-situ formation of ZIF-67 on the surface of AP-x supports resulted in significant changes in the ratios of Al_{Oh}^{3+}, Al_P^{3+} and Al_{Td}^{3+} sites (Fig. 2 F – 2 J). Compared with the AP-x samples, the ratios of Al_{Oh}^{3+} sites within ZAP-x samples generally increased. On the contrary, the ratios of Al_P^{3+} sites within ZAP-x samples decreased. This is probably because the Co atoms can occupy the unsaturated Al_P^{3+} sites to in-situ form ZIF-67 [19, 20,33–35]. Meanwhile, the reduced ratios of Al_{Td}^{3+} sites for ZAP-x samples (except ZAP-450) suggest that the tetrahedral sites can also anchor the Co atoms to form ZIF-67. More interestingly, the ratios of Al_P^{3+} sites in the CAP-x samples slightly increased compared with the ZAP-x samples (Fig. 2). This is probably due to the support surface reconstruction induced by the second calcination process (550 °C for 3 h). Such reconstruction has facilitated the migration of Co atoms from coordinatively unsaturated pentahedral sites to the tetrahedral sites or the saturated octahedral sites (See the changed ratios of Al_{Oh}^{3+} and Al_{Td}^{3+} sites for ZAP-x and CAP-x samples in Fig. 2). The ratios of Al_P^{3+} sites in the CAP-x samples are lower than those of AP-x samples, implying that the unsaturated Al_P^{3+} sites are still the essential binding sites for anchoring Co atoms to form interfacial Co_2AlO_4.

3.1.4. Chemical state analysis

The high-resolution XPS spectra of Co 2p and O 1 s for the CAP-x samples are depicted in Fig. 3. By fitting the Co $2p_{3/2}$ spectra, Co^{3+} species (779.7 eV) and Co^{2+} species (780.9 eV and 782.3 eV), satellite of

Co^{3+} (denoted as $Co_{sat.}^{3+}$, at 784.5 eV) and satellite of Co^{2+} (denoted as $Co_{sat.}^{2+}$, at 788.6 eV) can be easily identified (Fig. 3A – 3E) [36,37]. For the fitted O 1 s spectra of CAP-x samples, four sub-peaks at 529.9, 530.7, 531.7, and 532.9 eV are attributed to the Co-O bond, Al-O bond, defective oxygen (indexed as $O_{Def.}$), and surface-absorbed oxygen (indexed as $O_{Surf.}$) in CAP-x, respectively (Fig. 3F – 3 J) [14,38]. To facilitate the analysis, the total of Co-O and Al-O bonds are denoted as the lattice oxygen (indexed as $O_{Lat.}$).

The quantitative results of XPS spectra indicate that the contents of Co^{3+} species in the catalysts gradually decreased with the increase in pre-treatment temperature of supports. However, the trend was broken when the pre-treatment temperature increased to 1050 °C, and the highest content of Co^{3+} species (41.9%) was found in the CAP-1050. Unlike the Co^{3+} species, with the increase in pre-treatment temperature of supports, the contents of Co^{2+} species first increased from 32.0% (for CAP-Pristine) to 50.9% (for CAP-450), and then gradually decreased to 30.5% for CAP-1050 (Table S2). The ratio of Co^{3+}/Co^{2+} in CAP-Pristine is 1.3, much higher than those of CAP-450 (0.5), CAP-650 (0.5) and CAP-850 (0.4). The highest ratio of Co^{3+}/Co^{2+} (1.4) was observed for the CAP-1050 sample. Meanwhile, it is found that the change trend of $O_{Def.}$ is similar to that of Co^{2+} species.

3.1.5. Specific surface area

The specific surface areas of CAP-x samples were measured by means of N_2 adsorption/desorption isotherms (Fig. S2A – S2E). Results showed that BET surface area for CAP-Pristine, CAP-450, CAP-650, CAP-850 and CAP-1050 were 212.4, 190.8, 196.5, 114.7, and 51.5 m²/g, respectively. As a whole, BET surface area of the catalysts (except for CAP-650) decreased with the increased pre-treatment temperature for Al_2O_3-support (Fig. S2F).

3.1.6. Elemental distribution and coordination

TEM images of CAP-650 clearly show well dispersed Co-based species on the Al_2O_3 support. The crystallographic spacings of 2.86, 2.02, and 1.65 Å were observed in the selected area electron diffraction (SAED) pattern of CAP-650 (Figs. 4A and 4B), indicating the (220), (400), and (422) planes of Co_2AlO_4 (JCPDS#: 38–0814), respectively. This agrees with the investigations of UV–vis spectra. The blurred SAED implies that the crystallinity of Co_2AlO_4 is poor. The interplanar distance of 2.86 Å shown in HRTEM images is ascribed to the (220) plane of Co_2AlO_4 within CAP-650 (JCPDS#: 38–0814) (Figs. 4C and 4D). The Co_2AlO_4 is surrounded with much amorphous species and its crystal size is below < 10 nm. Furthermore, the element mappings verify the uniform dispersion of Co, Al, and O elements within CAP-650 (Fig. 4E – 4 H). Generally, poorly crystalline Co_2AlO_4 was formed on the Al_2O_3 support with high dispersion and ultrasmall crystal size.

We performed XANES and EXAFS characterization to further demonstrate the atomic-scale geometry structure of CAP-650. As shown in Fig. 4I, the normalized Co K-edge absorption threshold energy of CAP-650 is higher than that of Co foil and located between those of CoO and Co_3O_4, implying the Co valence state is between Co^{2+} and Co^{3+}. This finding is consistent with the XPS analysis (Section 3.1.4). The Fourier-transformed (FT) k^3-weighted EXAFS analysis and EXAFS fitting are summarized in Fig. 4J – 4 K, Table S3 and Text S6. Evidently, no Co-Co and Co-O-Co coordination peaks are detected in the FT-EXAFS spectrum of CAP-650, suggesting the absence of Co^0, CoO, and Co_3O_4 phases. The prominent peak at R = 1.83 Å (label A) is assigned to the first coordination shell of Co-O, while the other two weak peaks (label B and C) are ascribed to the Co-Al and Co-O-Al coordination, respectively. The bond distance of Co-Al between the adjacent Co and Al atoms is about 2.35 Å, while that of Co-O-Al between tetrahedral Co^{2+} and octahedral Al^{3+} atoms is about 2.99 Å [39]. The presence of Co-O-Al coordination further confirms that the strong metal-support interaction occurred between the Co species and Al_2O_3 support. The much higher coordination numbers of Co-O (2.8) and Co-O-Al (1.9) than that of Co-Al (1.1) imply that cobalt oxides are the dominant Co-based species within CAP-650.
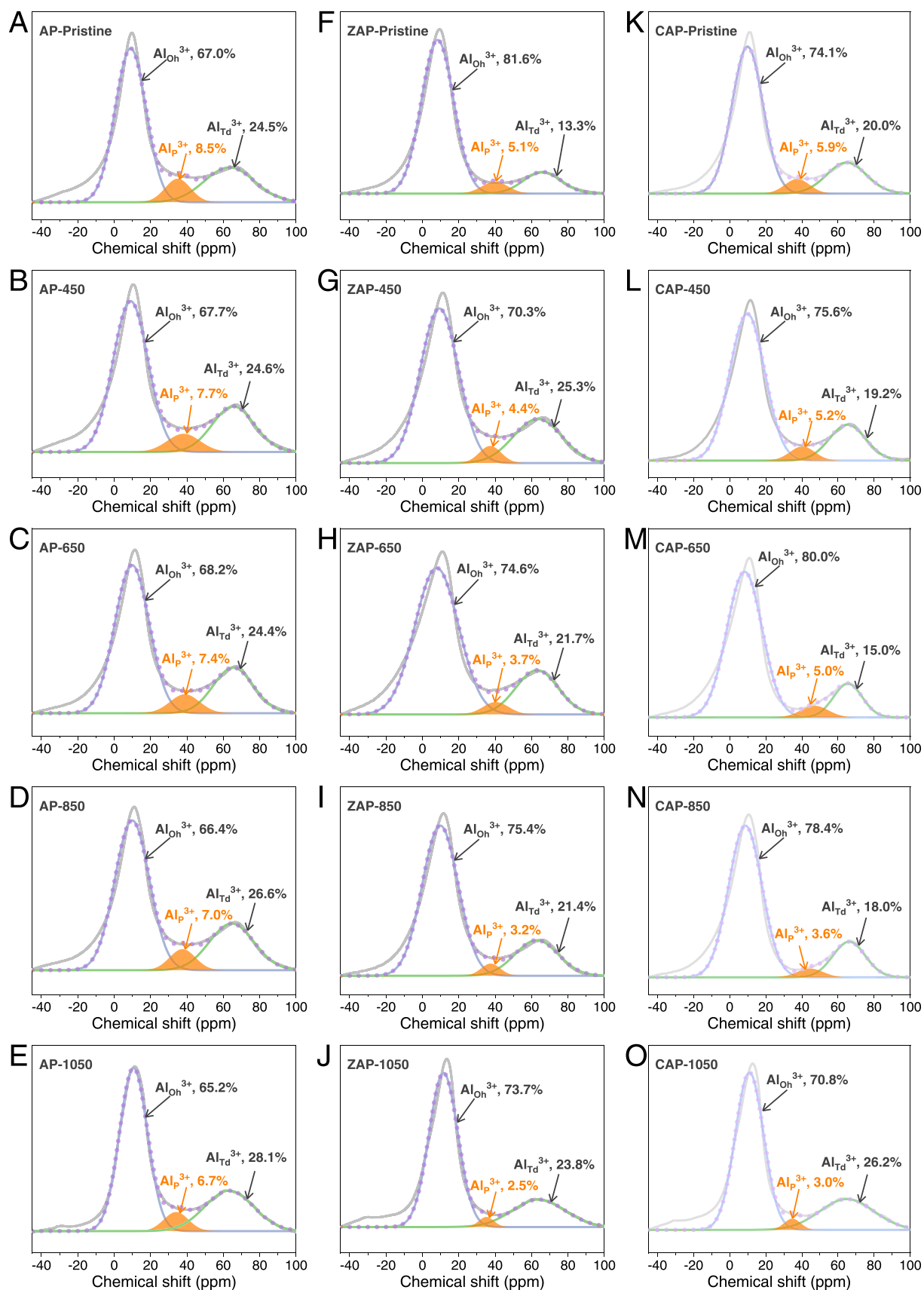
Fig. 2. 1D ^{27}Al MAS NMR spectra of AP-*x* samples (A – E), ZAP-*x* samples (F – J), and CAP-*x* samples (K – O) (*x* = 0, 450, 650, 850, 1050; Al_{Oh}^{3+}, Al_P^{3+}, and Al_{Td}^{3+} represent Al^{3+} cations in octa-, penta-, and tetrahedral coordination, respectively).
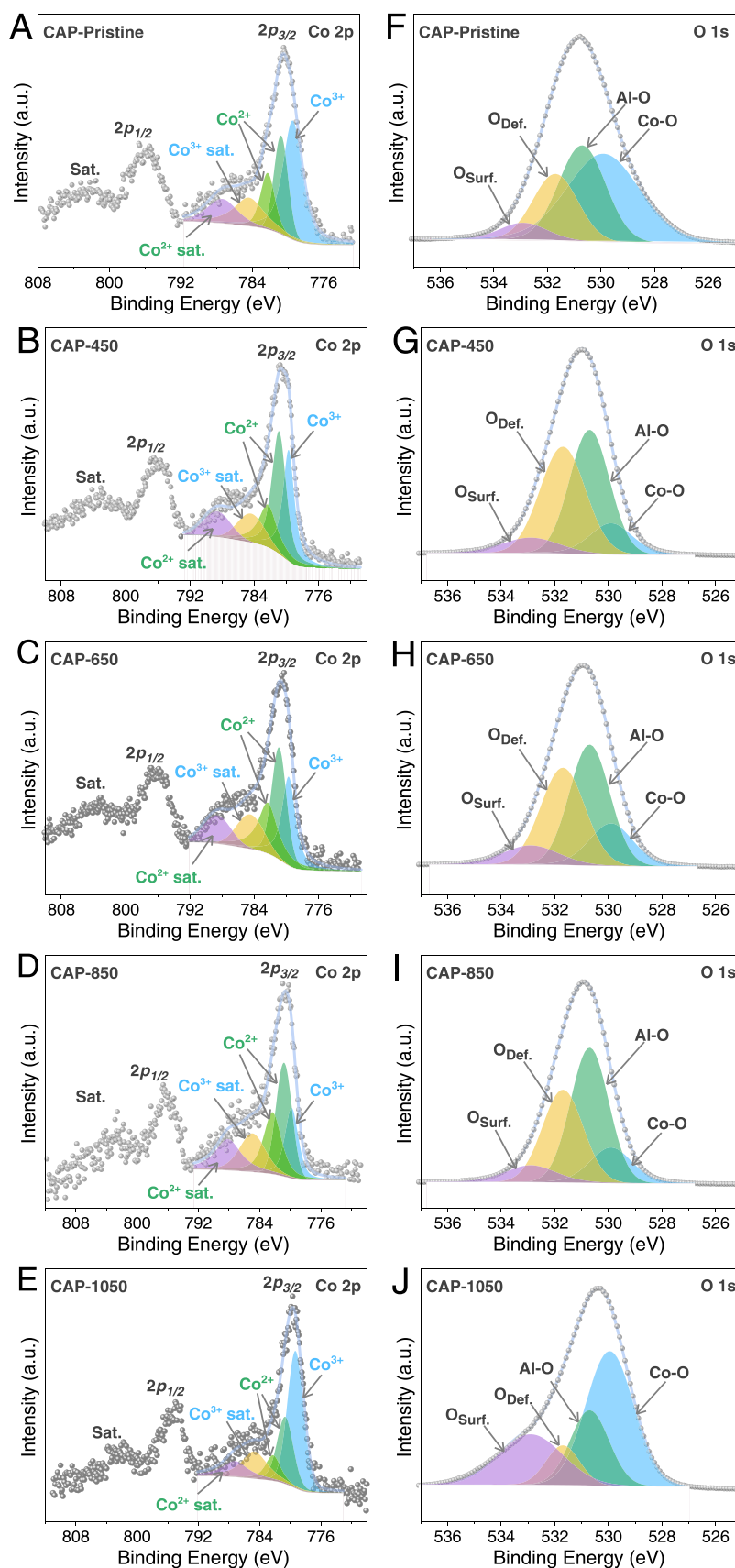
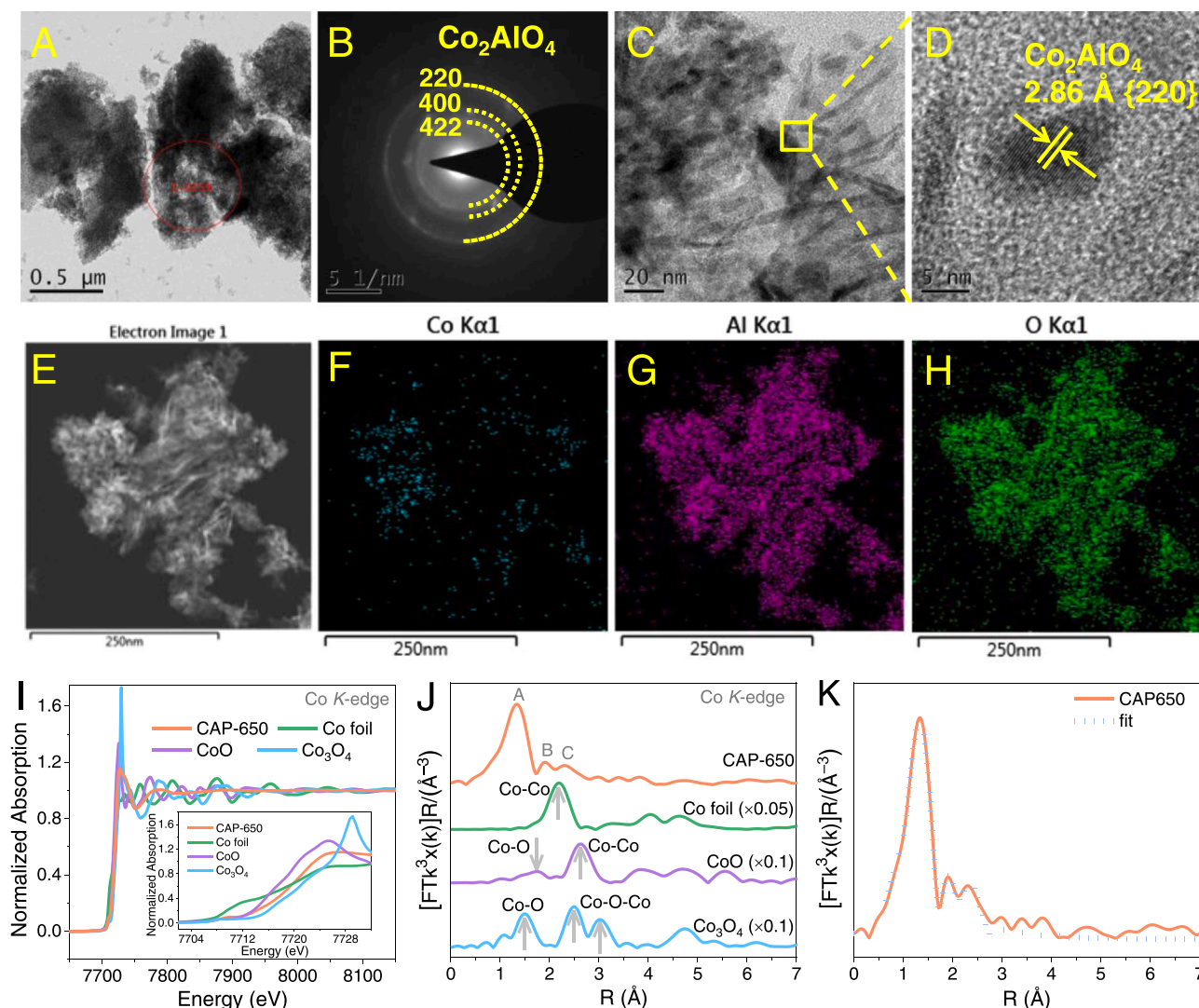**Fig. 3.** XPS analysis for Co 2p (A – E) and O 1 s (F – J) spectra of CAP-*x* samples.

Fig. 4. SAED pattern (A, B), HRTEM images (C, D) and TEM element mappings (E – H) of CAP-650. Normalized XANES (I) and Fourier transform curves of EXAFS (J) spectra at the Co K-edge of CAP-650, Co foil, CoO and Co_3O_4 samples, Co *K*-edge EXAFS analysis of CAP-650 at R space (K).

Generally, the EXAFS and EXAFS demonstrate that Co atoms can be stably anchored onto the Al_2O_3 support with strong metal-support interactions, which is significant to the formation of spinel Co_2AlO_4 phase.

3.1.7. Metal-support interaction analysis

As shown in Fig. S3, all of Co species depend linearly on the Co loading ($0.89 < R^2 < 0.98$), indicating that the Co loading largely affected the distribution of Co^{3+}, Co^{2+}, and Co^{3+}/Co^{2+} ratio. Fig. S4 shows different relationships between BET surface area and Co^{3+}, Co^{2+}, and Co^{3+}/Co^{2+} ratio. It is clear that the contents of Co^{3+} in CAP-*x* samples have higher correction with the catalyst surface area. The XPS and NMR characterizations were further analyzed to reveal the effect of support surface reconstruction on the interactions between Co elements and Al_2O_3 support. XPS analysis indicates the relationships between Co and O (Fig. 5A – 5E and Fig. S5). The distributions of Co species (i.e., Co^{2+} and Co^{3+}/Co^{2+}) largely depend on the contents of $O_{Def.}$, $O_{Lat.}$, $O_{surf.}$ and the ratio of $O_{Def.}/O_{Lat.}$. Generally, the "curved pattern" relationship between Co and O species can be better modeled by a binomial function with $R^2 > 0.94$ (Fig. 5A – 5E). As depicted in Fig. S5A – S5D, the nonlinear relationship between the ratio of $O_{Surf.}$ and Co^{3+} ($R^2 > 0.85$) is better than those between $O_{Def.}/O_{Lat.}$ and Co^{3+} ($R^2 < 0.83$), $O_{Def.}$ and Co^{3+} ($R^2 < 0.74$), or $O_{Lat.}$ and Co^{3+} ($R^2 < 0.70$). Compared with the inferior links between the content of $O_{Def.}$ (or $O_{Lat.}$) and the Co^{3+}/Co^{2+}

ratio (Fig. S5E – S5F, $R^2 < 0.86$), the ratio of $O_{Def.}/O_{Lat.}$ possesses a better correlation with the contents of Co^{2+} species and the ratio of Co^{3+}/Co^{2+} (Fig. 5D and Fig. S5G, $0.92 < R^2 < 0.98$). Meanwhile, Fig. 5E indicates that the Co^{3+}/Co^{2+} ratio was also highly dependent on the contents of $O_{Surf.}$ ($R^2 > 0.95$). These findings imply that most of Co elements preferred to deposit on the surface of the support and their distribution is highly dependent on the surface oxygen-containing groups.

From the XPS and NMR characterizations, the numbers of Al_P^{3+} not only affected the contents of Co species but also those of O species (except $O_{surf.}$, Fig. S6A), as confirmed by the well fitted curve relationship depicted in Fig. 5F – 5I and Fig. S6B – S6C ($R^2 > 0.83$). Also, the relationship between Al_{Oh}^{3+}(or Al_{Td}^{3+}) and Co/O species is poorly fitted in Fig. S6D – S6K ($0.39 < R^2 < 0.80$). These findings strongly indicate the crucial role of Al_P^{3+} in the formation of the catalysts. Combined with the discussion in Section 3.1.4, the pre-treatment of Al_2O_3 supports induced their surface reconstruction and steered the rearrangement of Al and O species within the supports. This is of great significance in anchoring Co atoms for in-situ formation of ZIF-67. As a whole, the Co atoms are anchored on the Al_P^{3+} sites of ZAP-*x* samples through oxygen bridges, which can be further converted into spinel Co_2AlO_4 composites via strong metal-support interactions under the calcination conditions (i.e., to form a Co-O-Al bond, as confirmed in Section 3.1.6).
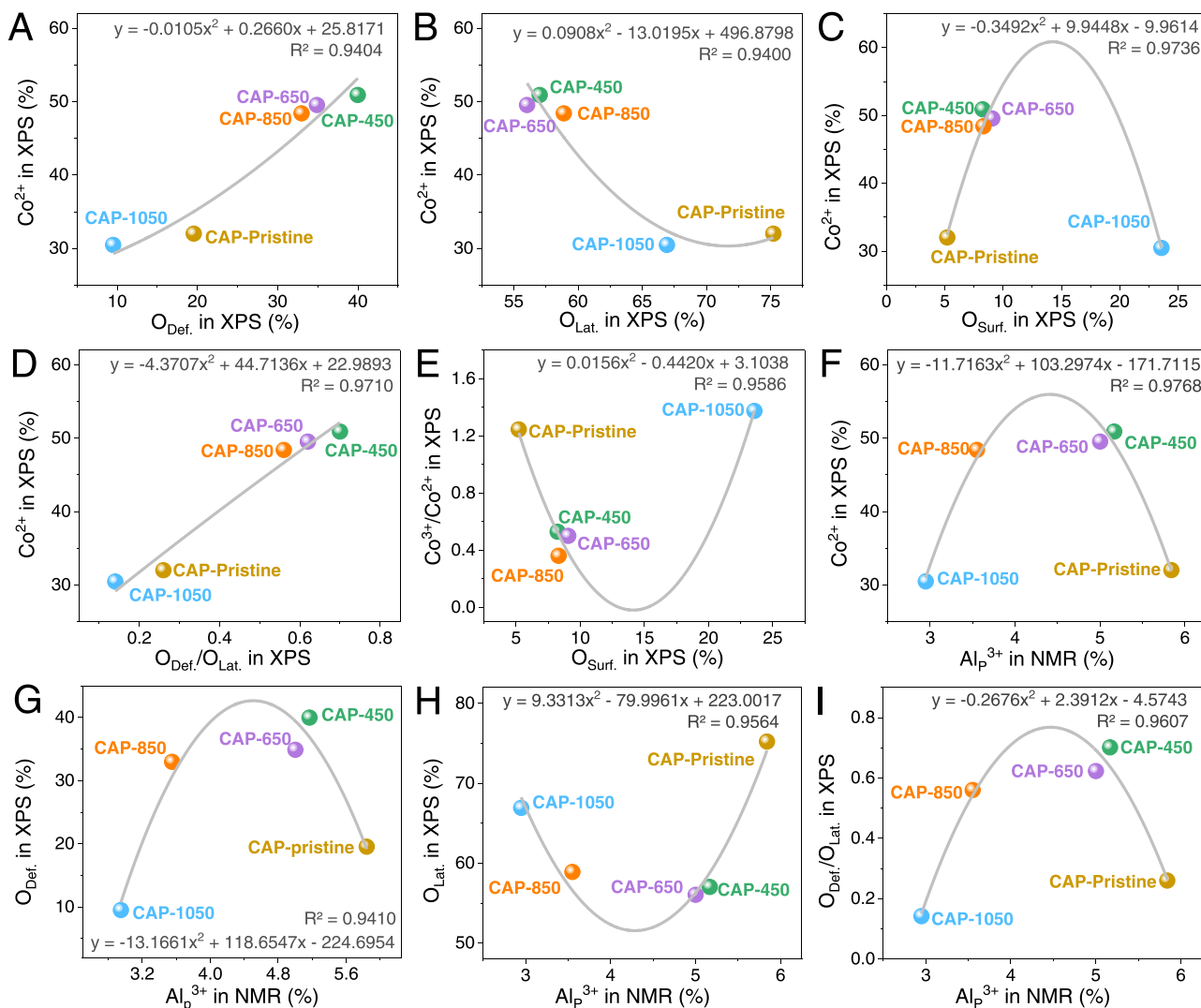
Fig. 5. The relationships between various structural parameters based on XPS and/or NMR analysis.

3.2. Reactivity characteristics in pollutant removal

Fig. 6A shows the reactivity of CAP-*x* in PMS activation to degrade AO7. Noted that AO7 removal caused by the oxidation of sole PMS was insignificant (Fig. S7). Within 25 min, 89.1% of AO7 (as a probe pollutant) was removed by CAP-Pristine-activated PMS. The corresponding first-order reaction rate constant (k_{obs}) for AO7 removal was determined as 8.5×10^{-2} min^{-1}. As expected, CAP-650 showed the best performance in PMS activation, as confirmed by the complete removal of AO7 (25 min) and the highest k_{obs} value of 1.7×10^{-1} min^{-1}. By contrast, the activities of CAP-450 and CAP-850 in PMS activation are slightly inferior to that of CAP-650. In detail, the removal efficiencies of AO7 within 25 min by the CAP-450/PMS and CAP-850/PMS systems are 98.6% and 96.2%, respectively, with the corresponding k_{obs} values of 1.6×10^{-1} and 1.2×10^{-1} min^{-1}, respectively. CAP-1050 exhibited the worst catalytic activity in PMS activation. The removal efficiency of AO7 by the CAP-1050/PMS system is about 51.7% within 25 min. Prolonging the reaction time to 45 min could slightly increase the removal efficiency to 66.3%. These results indicate that pre-treating the γ-Al$_2$O$_3$ support at suitable calcination condition (450–850 °C) is critical to optimizing and enhancing the catalytic activity of CAP-*x* series. Excessive calcination temperature (like 1050 °C) for the pre-treatment of γ-Al$_2$O$_3$ induces a negative impact on the activity of CAP-*x*. This can be confirmed by the lowest k_{obs} value for AO7 ($k_{obs} = 2.6 \times 10^{-2}$ min^{-1}),

which is accordingly 6- and 2-fold lower than those by CAP-650 and CAP-Pristine-based systems. In addition, the Co ions released from CAP-*x*/PMS system were also detected with the help of ICP-OES. Results show that there were no Co ions released from CAP-Pristine/CAP-1050 mediated reaction system, while that from CAP-450, CAP-650 and CAP-850 were 0.027, 0.090, and 0.022 mg/L, respectively.

3.3. Quantitative property-activity relationship

To understand the surface property-regulated catalytic activity of CAP-*x* in PMS activation, we probed the relationships between the Co loading/physicochemical parameters (based on XPS and NMR characterizations) and the k_{obs} values of AO7. As shown in Fig. S8 and Fig. 6B – 6 F, no linear relationship exists between Co loading/various physicochemical parameters and the k_{obs} values. Conversely, nonlinear relationships can be established with different binomial models to describe the removal kinetics of pollutants by CAP-*x* activated PMS. For example, the relationship between the Co loading and k_{obs} can be well-described by a binomial model with R^2 > 0.93 (Fig. S8A), suggesting the Co loading of CAP-*x* performs an important role in their catalytic activities. This is ascribed to the significant influences of Co loading on the distribution of Co^{3+}/Co^{2+} species (Fig. S3), which, in turn, determined the AO7 removal kinetics. As shown in Fig. S8B, the influence of catalyst surface area on AO7 removal is weaker than that of Co loading. The
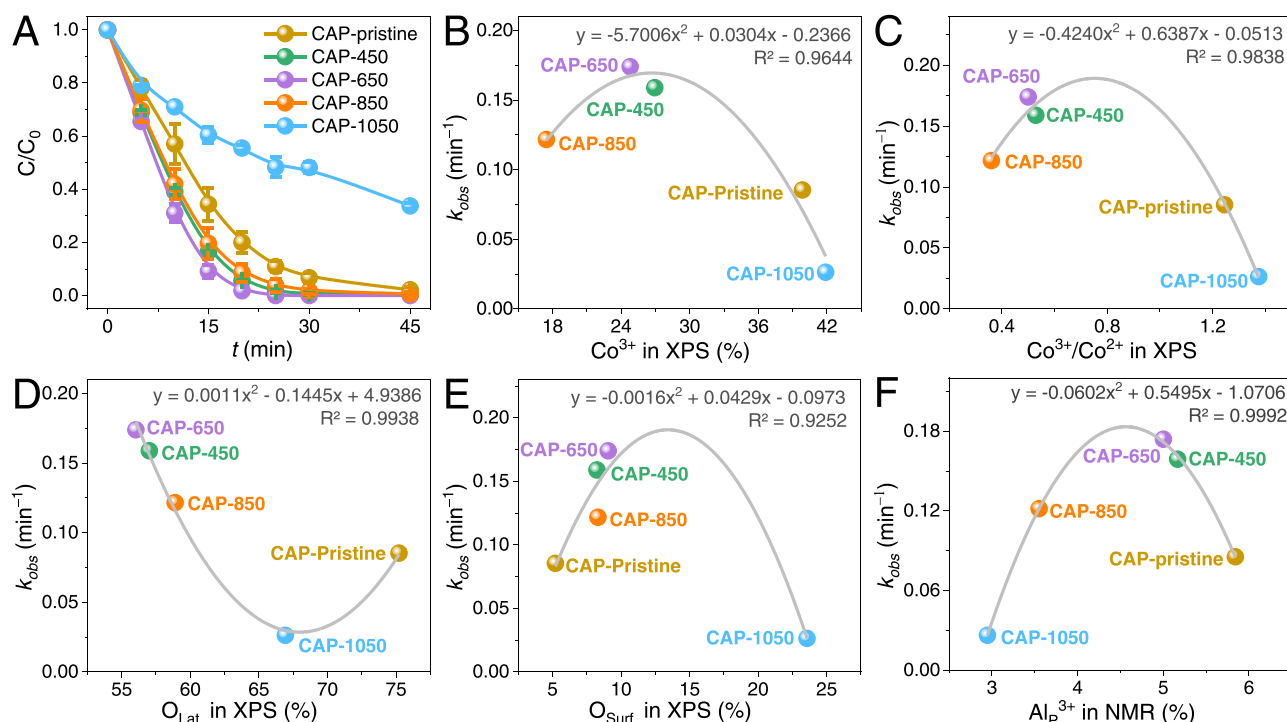
Fig. 6. AO7 removals in different oxidation processes (A) and the relationships between k_{obs} and various structural parameters (B – I) ([PMS] = 0.1 g/L, [CAP-x] = 20 g/L, [AO7] = 10 mg/L, pH = 5.95, T = 25 ± 1 °C).

specific activity (the k_{obs} values normalized to the catalyst surface area, Fig. S8C) was employed to further understand the intrinsic catalytic activity of CAP-x samples. It is apparent that the correlation of specific activity with Co loading is not strong in comparison with those of Co loading and k_{obs} (Fig. S8A and S8C). This indicates that the surface area is not the determining factor affecting the catalytic activity of CAP-x. This is probably due to the fact that the BET surface area is not equivalent to the real catalytically surface area access to the Fenton-like catalysis reaction, especially for the monolithic catalysts with mm-scale size. As shown in Fig. 6B, the contents of Co^{3+} and k_{obs} can be fitted by a binomial model with $R^2 > 0.96$, indicating that AO7 removal rate is highly dependent on the Co^{3+} contents within CAP-x samples. The effects of Co^{2+} contents on AO7 removal rate are weaker than those of Co^{3+} contents, as evidenced by their inferior fitting degree ($R^2 <$ 0.84) (Fig. S8D). Even so, their Co^{3+}/Co^{2+} ratio shows a high correlation with k_{obs} values ($R^2 > 0.98$, Fig. 6 C). These findings strongly suggest a decisive role of Co^{3+} species in the Co^{3+}/Co^{2+} ratio and therefore determine the performance of PMS activation. Also, different O species (i.e., $O_{Def.}$, $O_{Lat.}$ and $O_{Surf.}$) correlate well with the k_{obs} values ($R^2 > 0.92$) (shown in Fig. 6D – 6E and Fig. S8E – S8F). Although the single Co-O bond or Al-O bond showed an inferior relationship (Fig. S8G – S8H) with the k_{obs} values ($R^2 < 0.87$), their collection (i.e., $O_{Lat.}$) is highly correlated with the k_{obs} values ($R^2 > 0.99$) (Fig. 6D). This indicates that the O atoms exist in the Co-O-Al form and thus exhibit an indirect role in PMS activation. These results suggest that the oxygen species cannot serve as a decisive factor in PMS activation, but act as a bridge between Co species and the Al_2O_3 support. More likely, Co species were the active centers and directly decided the catalytic efficacy of the monolithic CAP-x. Compared with the correlation between Al_{Oh}^{3+} (Al_{Td}^{3+} or $Al_{Oh}^{3+}/Al_{Td}^{3+}$) and the k_{obs} values (Fig. S8I – S8K, $R^2 < 0.84$), the relationship between Al_P^{3+} and the k_{obs} values is significantly stronger (Fig. 6 F, $R^2 > 0.99$). This is because the unsaturated Al_P^{3+} can serve as an important binding site to tailor the formation of Co^{3+} and Co^{2+} species, thus regulating their catalytic activity in PMS activation. Notably, the number of Al_P^{3+} should be controlled within a suitable range. Excessive or insufficient Al_P^{3+} will negatively affect the activity of CAP-x (like CAP-Pristine or CAP-1050).

This probably results from the effects of Al_{Oh}^{3+} and Al_{Td}^{3+} on the formation of Co-based species on the surface of AP-Pristine or AP-1050, which could break the balanced ratio of Co^{3+}/Co^{2+} and ultimately affect the catalytic activity of CAP-x.

3.4. Recyclability and applicability

The reusability of CAP-650 in PMS activation was examined in six consecutive cycles without regeneration. After each use, CAP-650 pellets were separated by a stainless strainer, washed with DI water, and directly used in the next cycle. As indicated in Fig. 7A, CAP-650 pellets can retain their original catalytic activities in the first three runs. The activity of CAP-650 pellets was slightly reduced after the sixth reuse, with a high AO7 removal efficiency (93%) (Fig. 7B). This is acceptable because the active sites of CAP-650 pellets were inevitably covered by the by-products formed in the reuse experiments. As shown in Fig. 7B, the concentrations of released Co ions from CAP-650 over six recycles are much below the suggested value of 110 μg/L by the Water Quality Guidelines for Cobalt (British Columbia, 2004), which would not cause any biotoxicity for the aquatic life [40]. All the evidence indicates that the optimized CAP-650 is a robust catalyst for PMS activation in long-term operations.

The applicability of CAP-650 in catalytically activating PMS to remove different pollutants is shown in Fig. 7C. The dosage of PMS used here is 0.15 g/L. The removal efficiencies of CBZ, BPA, BPB, 2-CP and phenol, within 45 min, can reach 100%, 95.7%, 84.3%, 90.2% and 78.5%, respectively. The corresponding k_{obs} values are 7.2×10^{-2}, 6.3×10^{-2}, 3.9×10^{-2}, 4.8×10^{-2}, and 3.4×10^{-2} min^{-1}, respectively. These observations indicate an outstanding activity of CAP-650 in catalytically removing CBZ, BPA, 2-CP, BPB and phenol via PMS activation.

3.5. CAP-650-mediated PMS activation mechanisms

3.5.1. Types of active species

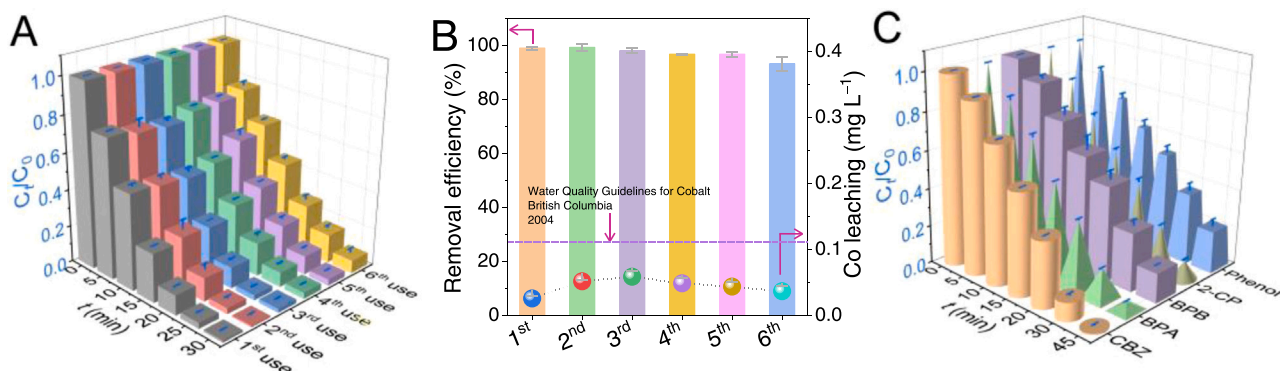As depicted in Fig. 8A – 8B, the catalytic activity of CAP-650 in PMS

Fig. 7. The reusability of CAP-650 toward PMS activation for AO7 removal (A, B), and degradation of various pollutants in CAP-650/PMS system (C) ([PMS] = 0.10 – 0.15 g/L, [CAP-650] = 20 g/L, [pollutant] = 10 mg/L, $pH_{CBZ, BPA, BPB, 2-CP, Phenol}$ = 6.70 ± 0.1, pH_{AO7} = 5.95, T = 25 ± 1 °C).
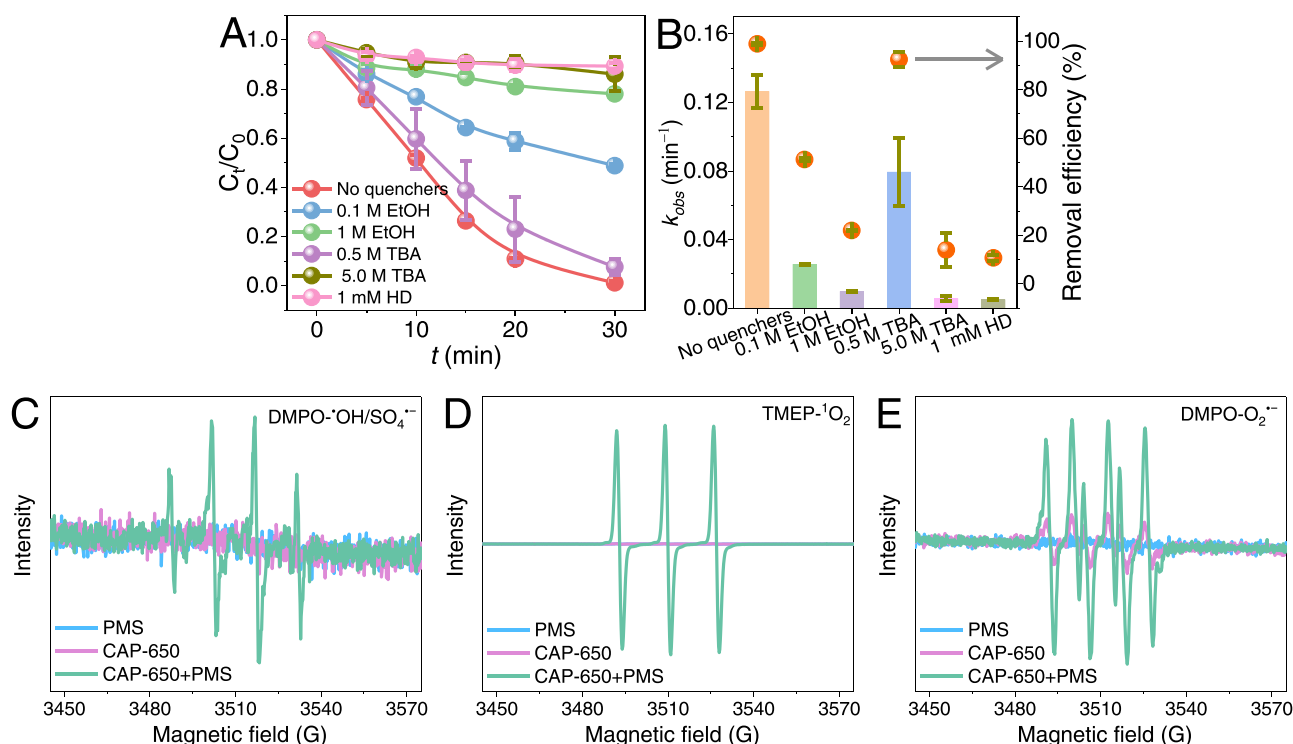

Fig. 8. Effects of various scavengers on AO7 removal by CAP-650/PMS (A – B) ([PMS] = 0.1 g/L, [CAP-650] = 20 g/L, [AO7] = 10 mg/L, pH = 5.95, T = 25 ± 1 °C); EPR spectra of DMPO-$^{\bullet}$OH/SO$_4^{\bullet-}$ adducts, TMEP-^{1}O$_2$ adducts and DMPO-O$_2^{\bullet-}$ adducts in the CAP-650/PMS system (C – E) ([DMPO] = 100 mM, [TEMP] = 100 mM, [CAP-650] = 0. 25 g/L, [PMS] = 0.2 g/L, pH = 7.0).

activation for pollutant removal was significantly inhibited by EtOH (0.1 and 1.0 M), TBA (0.5 and 5.0 M) and HD (1 mM). Compared with the scavengers-free case, the presence of 0.1 M EtOH (scavenging SO$_4^{\bullet-}$ and $^{\bullet}$OH simultaneously) decreased the removal kinetics of AO7 by 3.9 times. After adding 1 M EtOH to CAP-650/PMS system, only 22.0% of AO7 was removed within 30 min. These results imply that SO$_4^{\bullet-}$ and $^{\bullet}$OH might participate in AO7 degradation. However, EtOH cannot determine the individual role of SO$_4^{\bullet-}$ and $^{\bullet}$OH in pollutant removal, because EtOH can simultaneously react with both SO$_4^{\bullet-}$ ((1.6 – 7.7) × 10^7 M^{-1}s^{-1}) and $^{\bullet}$OH (1.9 × 10^9 M^{-1}s^{-1}) with high second-order reaction rate constants [41]. Thus, TBA was used to further differentiate the contributions of SO$_4^{\bullet-}$ and $^{\bullet}$OH due to its higher affinity of quenching $^{\bullet}$OH ((3.8 – 7.6) × 10^8 M^{-1}s^{-1}) than quenching SO$_4^{\bullet-}$ ((4 – 8.1) × 10^5 M^{-1}s^{-1}) [41]. Apparently, the inhibition effect of 0.5 M TBA was much weaker than 0.1 M EtOH, excluding the dominant role of $^{\bullet}$OH. Strangely, 5.0 M TBA dramatically decreased the catalytic activity of CAP-650/PMS system, as evidenced by the lower AO7 removal

efficiency. The enhanced inhibition is ascribed to the increased k_{obs} value of 5.0 M TBA with SO$_4^{\bullet-}$ ((2.0 – 4.1) × 10^6 s^{-1}), which is close to that of 0.1 M EtOH with SO$_4^{\bullet-}$ ((1.6 – 7.7) × 10^6 s^{-1}) [41]. Meanwhile, the slightly higher inhibition of 5 M TBA than 1 M EtOH further verifies the formation of $^{\bullet}$OH.

It is worthy of note that the presence of 1 M EtOH or 5 M TBA can hardly induce complete inhibition to AO7 degradation, indicating that other active species formed during PMS activation by CAP-650. Therefore, HD was also employed in the quenching experiments. Although HD is widely accepted as a scavenger of ^{1}O$_2$ (6.6 × 10^7 M^{-1}s^{-1}), HD can also quench SO$_4^{\bullet-}$ (5.0 × 10^9 M^{-1}s^{-1}) and $^{\bullet}$OH (2.5 × 10^9 M^{-1}s^{-1}) [41]. Considering this fact, 1 mM HD was used to make its k_{obs} value with SO$_4^{\bullet-}$ and $^{\bullet}$OH comparable to (or lower than) those of 0.1 M EtOH or 5 M TBA. The presence of 1 mM HD gave the most substantial inhibition to AO7 removal, suggesting that CAP-650 can also activate PMS to generate ^{1}O$_2$. The inhibition of 1 mM HD is stronger than that of 0.1 M EtOH, indicating a significant contribution of ^{1}O$_2$ to the AO7 removal.

The generation of $SO_4^{\bullet-}$, $^{\bullet}OH$ and $^1O_2$ were further verified by the EPR characterizations (Fig. 8C – 8D). The weaker signal of DMPO-$SO_4^{\bullet-}$ than that of DMPO-$^{\bullet}OH$ can be attributed to the short lifetime of DMPO-$SO_4^{\bullet-}$ in water and its easy conversion into DMPO-$^{\bullet}OH$ adducts [42,43]. Compared with the case of CAP-650 + PMS, there exist no signals for the cases of sole CAP-650 and PMS (Fig. 8C – 8D). This indicates that the formation of $SO_4^{\bullet-}$, $^{\bullet}OH$ and $^1O_2$ was due to the PMS activation by CAP-650. In addition, the formation of $O_2^{\bullet-}$ was also recorded by EPR (Fig. 8E). It is interesting to find that the sole CAP-650 possesses the ability of producing $O_2^{\bullet-}$. The combination of CAP-650 with PMS can induce more $O_2^{\bullet-}$ via its catalytic activation. Taking the results of quenching experiments and EPR characterizations into consideration, it is concluded that CAP-650 can activate PMS to generate $SO_4^{\bullet-}$, $^{\bullet}OH$, $^1O_2$ and $O_2^{\bullet-}$ simultaneously, among which $SO_4^{\bullet-}$ and $^1O_2$ are the dominant reactive species responsible for AO7 removal.

3.5.2. Origin of CAP-650 in activating PMS

To reveal the mechanism of PMS activation over CAP-650 to form active species, we analyzed the changes of surface properties of CAP-650 before and after the reaction by soft XAS, XPS and UV–vis characterizations. Fig. 9A shows the Co L-edge spectra with L_2 branch (transition from Co $2p_{1/2}$ into Co 3d orbital) and L_3 branch (transition from Co $2p_{3/2}$ into Co 3d orbital). The peak of the Co-L_3 edge for used CAP-650 moved toward a higher energy position (779.3 eV) compared with the fresh one (779.2 eV), suggesting an increased Co valence state within the used one [44]. As demonstrated in Fig. 9B, the O K-edge XAS spectra of fresh and used CAP-650 indicated the O 2p-Co 3d hybridized state (532.1 eV) and O 2p-Co 4s4p hybridized state (541.4 eV) [45]. The peak intensity of 532.1 eV increased slightly for the used CAP-650, suggesting the slightly increased Co 3d electrons in the hybridized orbitals [45–47]. To examine the change in the valence state and/or spin state of Co elements within CAP-650 before and after use, we simulated the XAS spectra at Co-L_3 edge via superposing the references of cobalt oxides. As shown in Fig. 9C – 9D, the spectra can be fitted with the Co^{2+}-based species in the HS-Co_{Td}^{2+} and HS-Co_{Oh}^{2+} coordination [48], and the Co_{Oh}^{3+} species in the LS and HS state (denoted as LS-Co_{Oh}^{3+} and HS-Co_{Oh}^{3+}) [49,50]. Quantitative

analysis of XAS spectra indicates an increased valance state of Co elements from 2.55 + to 2.60 + for the used CAP-650 [49]. The amounts of HS-Co_{Td}^{2+} and LS-Co_{Oh}^{3+} for the used CAP-650 were decreased by 5.6% and 0.4%, respectively, while those of HS-Co_{Oh}^{2+} and HS-Co_{Oh}^{3+} were increased by 0.6% and 5.4%, respectively. We suppose that the transformation of HS-Co_{Td}^{2+} into HS-Co_{Oh}^{3+} would mediate the electron transfer for PMS activation.

Despite the insignificant change in the morphology (Fig. S9) and the crystalline phase (Fig. S1B), remarkable changes had been observed for the UV–vis spectra of CAP-650 before and after activating PMS (Fig. 9E). For instance, when the CAP-650 samples were subjected to the PMS activation, their two typical bands at 239 and 411 nm shifted to 228 and 399 nm, respectively. Such remarkable shifts suggest an increased octahedral coordination capacity/number of Co^{3+} ions within CAP-650 over PMS activation [27,29]. This can be verified by the increased contents of Co^{3+} from 24.8% (for the fresh CAP-650) to 28.2% (for the used CAP-650) (Figs. 3C and 9F). The band at 641 nm was observed for both fresh and used CAP-650, implying the robustness of the tetrahedral coordination field of Co^{2+} ions over PMS activation [25,27]. The decreased contents of Co^{2+} from 49.5% to 39.4% (Figs. 3C and 9F), the increased ratio of Co^{3+}/Co^{2+} (from XPS spectra) and the transformation of HS-Co_{Td}^{2+} into LS-Co_{Oh}^{3+} (Figs. 9C and 9D) suggest that the electron transfer occurred for PMS activation [51].

The theoretical calculations were performed to further reveal the underlying mechanisms on how CAP-650 activates PMS to form the dominant oxidants of $SO_4^{\bullet-}$ and $^1O_2$ For the clean $Co_2AlO_4(220)$ surface, Co_{4c} is the dominating active site as shown in Fig. 10A, based on which SO_5^{2-} has been adsorbed via dual Co-O bonding with large adsorption energy $E_{ads} = -2.59$ eV. Most importantly, SO_5^* can further dissociate as SO_4^* and O^* with an energy cost of -0.40 eV, as presented in Fig. 10B. The dissociation origins from the high activity Co_{4c}, which presents with high spin and a large amount of occupied states being close to Fermi energy, as labeled by red arrow in the calculated density of states in Fig. 10C. Under such case, both $SO_4^{\bullet-}$ and $1/2\,^1O_2$ can be generated by Eq. (1) — (4). As indicated by the reaction energy (ΔE), these elementary steps are energetically favorable. It is also worth to
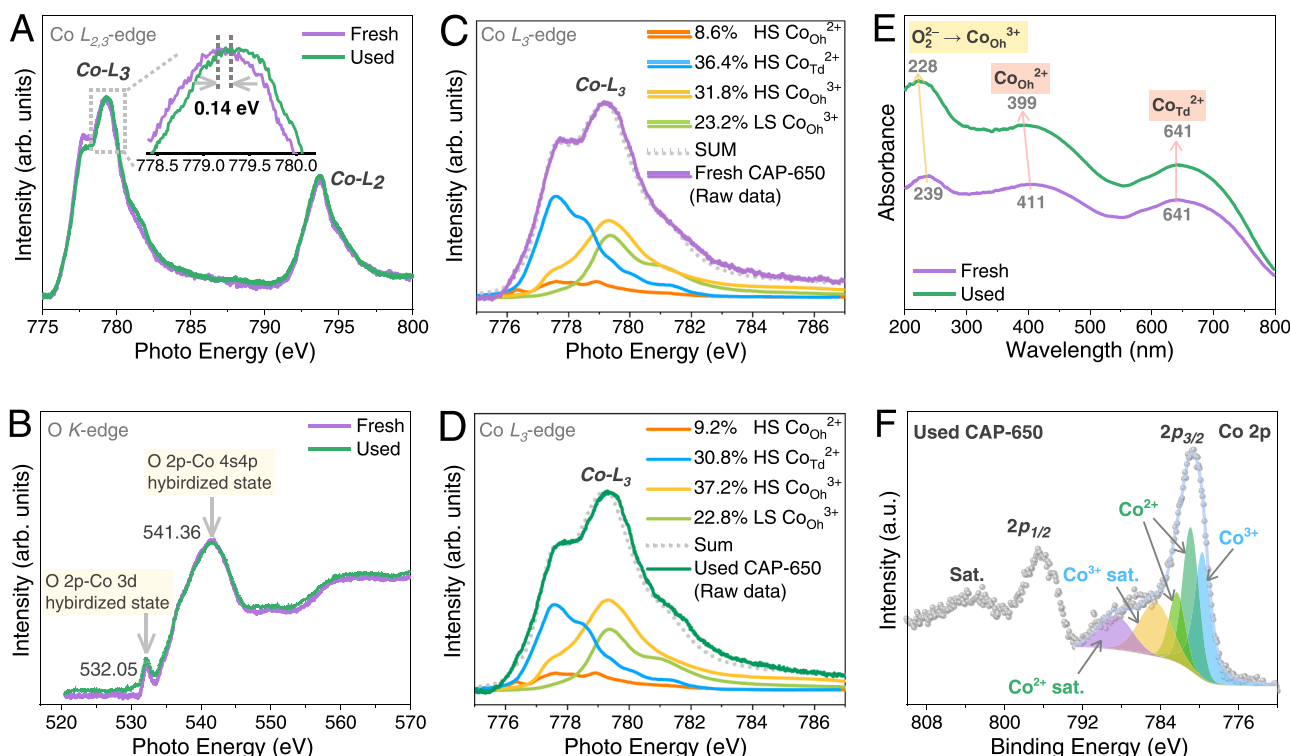

Fig. 9. The Co L-edge and O K-edge XAS spectra (A – D), UV–vis spectra (E), and Co 2p spectra of fresh and used CAP-650 (F).
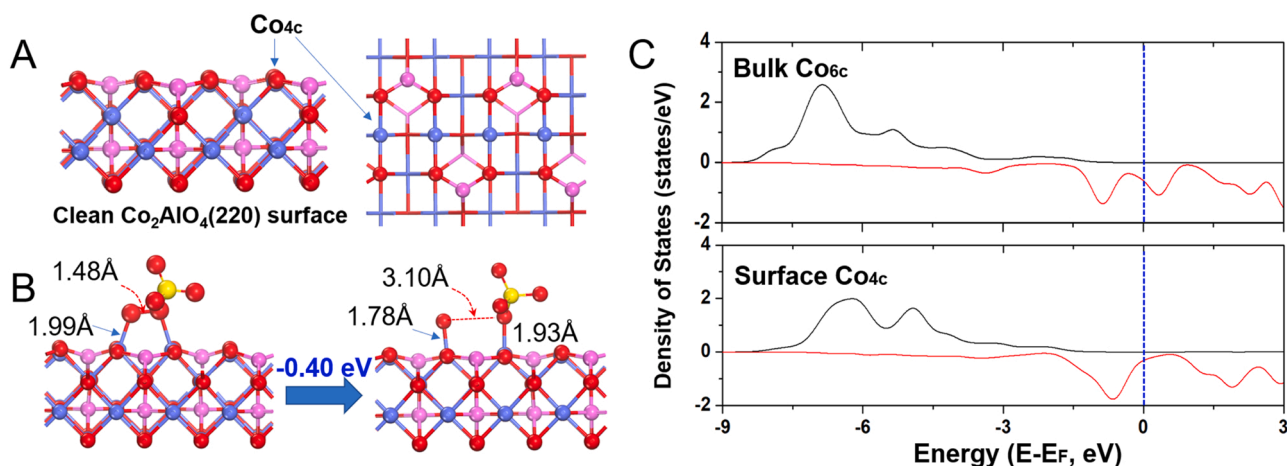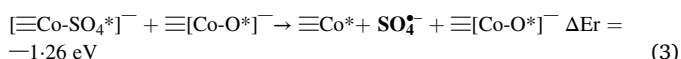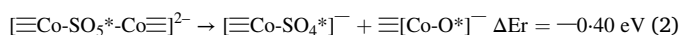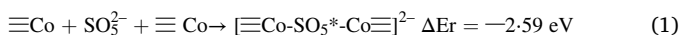
Fig. 10. DFT calculations of PMS adsorption and electronic structures. (A) Optimized (220) surface; (B) two geometries (SO_5* and SO_4* + O*) of PMS adsorption with key bond lengths; (C) local density of states for bulk Co6c and surface Co4c.

mention that the final surface charge (see [≡Co*]⁻ in Eq. (4)) can be canceled because each PMS molecule introduces a single proton (H⁺) before being fixed from the solution to the surface.

$$\equiv Co + SO_5^{2-} + \equiv Co \rightarrow [\equiv Co\text{-}SO_5\text{*-}Co\equiv]^{2-} \quad \Delta Er = -2 \cdot 59 \text{ eV} \quad (1)$$

$$[\equiv Co\text{-}SO_5\text{*-}Co\equiv]^{2-} \rightarrow [\equiv Co\text{-}SO_4\text{*}]^- + \equiv[Co\text{-}O\text{*}]^- \quad \Delta Er = -0 \cdot 40 \text{ eV} \quad (2)$$

$$[\equiv Co\text{-}SO_4\text{*}]^- + \equiv[Co\text{-}O\text{*}]^- \rightarrow \equiv Co\text{*} + \mathbf{SO_4^{\bullet-}} + \equiv[Co\text{-}O\text{*}]^- \quad \Delta Er = -1 \cdot 26 \text{ eV} \quad (3)$$

$$\equiv[Co\text{-}O\text{*}]^- \rightarrow [\equiv Co\text{*}]^- + 1/2^1O_2 \quad \Delta Er = -1 \cdot 80 \text{ eV} \quad (4)$$

In addition, the corresponding degradation pathways and the toxicity of the oxidation products of AO7 by CAP-650/PMS has also been studied and the methods can be found in Text S7. As detected by HPLC/MS/MS, nine kinds of by-products with m/z of 328, 174, 265, 166, 194, 138, 208, 202 and 344 were identified in the MS spectra with positive or negative modes (refer to Table S4 for the details). Hydrolysis of AO7 resulted in the formation of P328 (12.80%), which can be further transformed into P202 (43.81%) via N＝N cleavage, oxygen addition and dehydrogenation. Obviously, this is the major pathway of AO7 degradation by CAP-650/PMS system. The chain cleavage, repeated oxidation and decarboxylation on *TS5* led to the third most important product of P138 (11.44%). The rest of products, like P174, P265, P166, P194, P208 and P344, can also be formed via the routes depicted in Fig. S10. As predicted by T.E.S.T. software, besides P328, the rest of products have lower developmental toxicity than parent AO7, and the normalized total value of all products is 0.56, much lower than that of AO7 (0.98) (Fig. S11A). This suggests the oxidation of AO7 by CAP-650/PMS helps to reduce the developmental toxicity of AO7 to the creatures. Even though P174 and P265 showed higher mutagenicity values than AO7, the normalized total mutagenicity values for all products are lower than that of AO7. This indicates that CAP-650/PMS system is conducive to reduce the mutagenicity risk of parent AO7 (Fig. S11B). As for the acute toxicity for rat, unfortunately, all products showed lower *Oral rat* LD50 values than parent AO7, and the normalized total *Oral rat* LD50 is 2959.76 mg/kg, indicating that AO7 degradation by CAP-650/PMS slightly increased the toxicity to the rat (Fig. S11C).

4. Conclusions

In conclusion, we provided a support surface reconstruction strategy to modulate millimeter-scaled Co_2AlO_4 @Al_2O_3 catalysts with tunable Co^{2+}/Co^{3+} redox centers via the strong metal-support interactions. The quantitative property-activity relationships for the millimeter-scaled Co_2AlO_4 @Al_2O_3-mediated PMS activation had been systematically

revealed by the combined UV–vis, NMR, XPS, XANES and EXAFS characterizations. The distributions of tetrahedral, octahedral and pentacoordinate Al^{3+} sites on the Al_2O_3 supports can be tuned by simply altering the calcination temperature. The rearranged tetrahedral and pentacoordinate Al^{3+} sites can anchor cobalt ions to form Co_2AlO_4. The activity of Co_2AlO_4 @Al_2O_3 millispheres in activating PMS was non-linearly correlated with the Co^{3+}/Co^{2+} ratio, the concentrations of lattice O and pentacoordinate Al^{3+}. The support surface reconstruction-coordinated Co^{3+}/Co^{2+} redox centers within Co_2AlO_4 @Al_2O_3 milli-spheres showed desirable catalytic activity, stability and reusability for removing a diversity of pollutants. The activity origin of Co_2AlO_4 @Al_2O_3 catalysts lies in their exposed (220) surface with HS-Co_{Td}^{2+} and LS-Co_{Oh}^{3+}, which can activate PMS to produce the dominant $SO_4^{\bullet-}$ and $^1O_2$ simultaneously via electron-transfer processes. This work will unleash the potential of developing support surface reconstruction strategies to synthesize/modulate millimeter-scaled catalysts with desirable geometric/electronic features for efficient water purification.

CRediT authorship contribution statement

Min-Ping Zhu: Conceptualization, Investigation, Methodology, Formal analysis, Visualization, Writing – original draft. **Jia-Cheng E. Yang**: Supervision, Conceptualization, Visualization, Writing – review & editing, Funding acquisition. **Xiaoguang Duan, Baoling Yuan and Shaobin Wang**: Writing – review & editing. **Chenghua Sun and Daqin Guan**: Methodology, Writing – review & editing. **Darren Delai Sun**: Supervision, Writing – review & editing. **Ming-Lai Fu**: Supervision, Resources, Writing – review & editing, Funding acquisition.

Declaration of Competing Interest

The authors declare that they have no known competing financial interests or personal relationships that could have appeared to influence the work reported in this paper.

Data availability

The data that has been used is confidential.

Acknowledgements

Appendix A. Supporting information

Supplementary data associated with this article can be found in the online version at doi:10.1016/j.apcatb.2023.122570.

References

[1] Y. Yao, H. Hu, H. Yin, M. Yu, H. Zheng, Y. Zhang, S. Wang, Phase change on stainless-steel mesh for promoting sulfate radical formation via peroxymonosulfate oxidation, Appl. Catal. B Environ. 278 (2020) 119333.

[2] Z. Wu, Y. Wang, Z. Xiong, Z. Ao, S. Pu, G. Yao, B. Lai, Core-shell magnetic Fe_3O_4@Zn/Co-ZIFs to activate peroxymonosulfate for highly efficient degradation of carbamazepine, Appl. Catal. B Environ. 277 (2020), 119136.

[3] L. Lai, H. Ji, H. Zhang, R. Liu, C. Zhou, W. Liu, Z. Ao, N. Li, C. Liu, G. Yao, B. Lai, Activation of peroxydisulfate by V-Fe concentrate ore for enhanced degradation of carbamazepine: surface =V(III) and =V(IV) as electron donors promoted the regeneration of =Fe(II), Appl. Catal. B Environ. 282 (2021) 119559.

[4] Q. Zhao, Z. Zhao, R. Rao, Y. Yang, S. Ling, F. Bi, X. Shi, J. Xu, G. Lu, X. Zhang, Universitetet i Oslo-67 (UiO-67)/graphite oxide composites with high capacities of toluene: synthesis strategy and adsorption mechanism insight, J. Colloid Interfaces Sci. 627 (2022) 385–397.

[5] C. Huang, Y. Zhang, X. Li, H. Cao, Y. Guo, C. Zhang, Mn-incorporated Co_3O_4 bifunctional electrocatalysts for zinc-air battery application: an experimental and DFT study, Appl. Catal. B Environ. 319 (2022) 121909.

[6] J. Chen, Y. Yang, S. Zhao, F. Bi, L. Song, N. Liu, J. Xu, Y. Wang, X. Zhang, Stable black phosphorus encapsulation in porous mesh-like UiO-66 promoted charge transfer for photocatalytic oxidation of toluene and o-dichlorobenzene: performance, degradation pathway, and mechanism, ACS Catal. 12 (2022) 8069–8081.

[7] Y. Yang, X. Li, B. Jie, Z. Zheng, J. Li, C. Zhu, S. Wang, J. Xu, X. Zhang, Electron structure modulation and bicarbonate surrounding enhance Fenton-like reactions performance of Co-Co PBA, J. Hazard. Mater. 437 (2022) 129372.

[8] M. Kohantorabi, S. Giannakis, G. Moussavi, M. Bensimon, M.R. Gholami, C. Pulgarin, An innovative, highly stable Ag/ZIF-67@GO nanocomposite with exceptional peroxymonosulfate (PMS) activation efficacy, for the destruction of chemical and microbiological contaminants under visible light, J. Hazard. Mater. 413 (2021), 125308.

[9] J. Li, W. Zhu, Y. Gao, P. Lin, J. Liu, J. Zhang, T. Huang, The catalyst derived from the sulfurized Co-doped metal–organic framework (MOF) for peroxymonosulfate (PMS) activation and its application to pollutant removal, Sep. Purif. Technol. 285 (2022) 120362.

[10] C. Zhao, B. Liu, X. Li, K. Zhu, R. Hu, Z. Ao, J. Wang, A. Co–Fe, Prussian blue analogue for efficient Fenton-like catalysis: the effect of high-spin cobalt, Chem. Commun. 55 (2019) 7151–7154.

[11] Y. Zhang, F. Liu, Z. Yang, J. Qian, B. Pan, Weakly hydrophobic nanoconfinement by graphene aerogels greatly enhances the reactivity and ambient stability of reactivity of MIL-101-Fe in Fenton-like reaction, Nano Res. 14 (2021) 2383–2389.

[12] D. Chen, Q. Bai, T. Ma, X. Jing, Y. Tian, R. Zhao, G. Zhang, Stable metal–organic framework fixing within zeolite beads for effectively static and continuous flow degradation of tetracycline by peroxymonosulfate activation, Chem. Eng. J. 435 (2022) 134916.

[13] K. Andrew Lin, H. Chang, B. Chen, Multi-functional MOF-derived magnetic carbon sponge, J. Mater. Chem. A 4 (2016) 13611–13625.

[14] Y. Bao, W. Oh, T. Lim, R. Wang, R.D. Webster, X. Hu, Surface-nucleated heterogeneous growth of zeolitic imidazolate framework – a unique precursor towards catalytic ceramic membranes: synthesis, characterization and organics degradation, Chem. Eng. J. 353 (2018) 69–79.

[15] M. Zhu, J.E. Yang, X. Duan, D. Zhang, S. Wang, B. Yuan, M. Fu, Interfacial $CoAl_2O_4$ from ZIF-67@γ-Al_2O_3 pellets toward catalytic activation of peroxymonosulfate for metronidazole removal, Chem. Eng. J. (2020), 125339.

[16] M. Zhu, J.E. Yang, X. Duan, S. Wang, D.D. Sun, B. Yuan, M. Fu, Engineered Co_2AlO_4/$CoAl_2O_4$@Al_2O_3 monolithic catalysts for peroxymonosulfate activation: Co^{3+}/Co^{2+} and O_{Defect}/$O_{Lattice}$ ratios dependence and mechanism, Chem. Eng. J. 409 (2021), 128162.

[17] A.S. Ivanova, E.M. Slavinskaya, R.V. Gulyaev, V.I. Zaikovskii, I.G. Stonkus, L. M. Danilova, I.A. Plyasova, A.I. Polukhina, Metal–support interactions in Pt/Al_2O_3 and Pd/Al_2O_3 catalysts for CO oxidation, Appl. Catal. B Environ. 97 (2010) 57–71.

[18] M. Wu, W. Li, X. Zhang, F. Xue, T. Yang, L. Yuan, Penta-coordinated Al^{3+} stabilized defect-rich ceria on Al_2O_3 supported palladium catalysts for lean methane oxidation, Chemcatchem 13 (2021) 3490–3500.

[19] J.H. Kwak, J. Hu, D. Mei, C. Yi, D.H. Kim, C.H.F. Peden, L.F. Allard, J. Szanyi, Coordinatively unsaturated Al^{3+} centers as binding sites for active catalyst phases of platinum on γ-Al_2O_3, Science 325 (2009) 1670–1673.

[20] W. Liu, S. Yang, Q. Zhang, T. He, Y. Luo, J. Tao, D. Wu, H. Peng, Insights into flower-like Al_2O_3 spheres with rich unsaturated pentacoordinate Al^{3+} sites stabilizing Ru-CeO_x for propane total oxidation, Appl. Catal. B Environ. 292 (2021), 120171.

[21] X. Shao, X. Li, J. Ma, R. Zhang, H. He, Terminal hydroxyl groups on Al_2O_3 supports influence the valence state and dispersity of Ag nanoparticles: implications for ozone decomposition, ACS Omega 6 (2021) 10715–10722.

[22] Y. Zhang, Y. Zu, D. He, J. Liang, L. Zhu, Y. Mei, Y. Luo, The tailored role of "defect" sites on γ-alumina: a key to yield an efficient methane dry reforming catalyst with superior nickel utilization, Appl. Catal. B Environ. 315 (2022) 121539.

[23] Z. Zhao, D. Xiao, K. Chen, R. Wang, L. Liang, Z. Liu, I. Hung, Z. Gan, G. Hou, Nature of five-coordinated Al in γ-Al_2O_3 revealed by ultra-high-field solid-state NMR, ACS Cent. Sci. (2022).

[24] K.J.D. MacKenzie, J. Temuujin, K. Okada, Thermal decomposition of mechanically activated gibbsite, Thermochim. Acta 327 (1999) 103–108.

[25] S. Velu, K. Suzuki, S. Hashimoto, N. Satoh, F. Ohashi, S. Tomura, The effect of cobalt on the structural properties and reducibility of CuCoZnAl layered double hydroxides and their thermally derived mixed oxides, J. Mater. Chem. 11 (2001) 2049–2060.

[26] C. Maurizio, N. El Habra, G. Rossetto, M. Merlini, E. Cattaruzza, L. Pandolfo, M. Casarin, XAS and GIXRD study of Co sites in $CoAl_2O_4$ layers grown by MOCVD, Chem. Mater. 22 (2010) 1933–1942.

[27] S. Kurajica, J. Popović, E. Tkalčec, B. Gržeta, V. Mandić, The effect of annealing temperature on the structure and optical properties of sol–gel derived nanocrystalline cobalt aluminate spinel, Mater. Chem. Phys. 135 (2012) 587–593.

[28] C.M. Álvarez-Docio, J.J. Reinosa, A. Del Campo, J.F. Fernández, 2D particles forming a nanostructured shell: a step forward cool NIR reflectivity for $CoAl_2O_4$ pigments, Dyes Pigment. 137 (2017) 1–11.

[29] L. Van de Water, G. Bezemer, J. Bergwerff, M. Versluijs-Helder, B. Weckhuysen, K. De Jong, Spatially resolved UV–vis microspectroscopy on the preparation of alumina-supported Co Fischer–Tropsch catalysts: linking activity to Co distribution and speciation, J. Catal. 242 (2006) 287–298.

[30] C. Wan, M.Y. Hu, N.R. Jaegers, D. Shi, H. Wang, F. Gao, Z. Qin, Y. Wang, J.Z. Hu, Investigating the surface structure of γ-Al_2O_3 supported WO_x catalysts by high field ^{27}Al MAS NMR and electronic structure calculations, J. Phys. Chem. C 120 (2016) 23093–23103.

[31] S. Xu, N.R. Jaegers, W. Hu, J.H. Kwak, X. Bao, J. Sun, Y. Wang, J.Z. Hu, High-Field one-dimensional and two-dimensional ^{27}Al magic-angle spinning nuclear magnetic resonance study of θ-, δ-, and γ-Al_2O_3 dominated aluminum oxides: toward understanding the Al sites in γ-Al_2O_3, ACS Omega 6 (2021) 4090–4099.

[32] J. Yan, M.C. Kung, W.M.H. Sachtler, H.H. Kung, Co/Al_2O_3 lean NO_x reduction catalyst, J. Catal. 172 (1997) 178–186.

[33] X. Yang, Q. Li, E. Lu, Z. Wang, X. Gong, Z. Yu, Y. Guo, L. Wang, Y. Guo, W. Zhan, J. Zhang, S. Dai, Taming the stability of Pd active phases through a compartmentalizing strategy toward nanostructured catalyst supports, Nat. Commun. 10 (2019) 1611.

[34] H. Duan, R. You, S. Xu, Z. Li, K. Qian, T. Cao, W. Huang, X. Bao, Pentacoordinated Al^{3+}-stabilized active Pd structures on Al_2O_3-coated palladium catalysts for methane combustion, Angew. Chem. Int. Ed. 131 (2019) 12171–12176.

[35] D. Mei, J.H. Kwak, J. Hu, S.J. Cho, J. Szanyi, L.F. Allard, C.H.F. Peden, Unique role of anchoring penta-coordinated Al^{3+} sites in the sintering of γ-Al_2O_3 -supported Pt catalysts, J. Phys. Chem. Lett. (2010) 2688–2691.

[36] S. Mo, Q. Zhang, Q. Ren, J. Xiong, M. Zhang, Z. Feng, D. Yan, M. Fu, J. Wu, L. Chen, D. Ye, Leaf-like Co-ZIF-L derivatives embedded on Co_2AlO_4/Ni foam from hydrotalcites as monolithic catalysts for toluene abatement, J. Hazard. Mater. 364 (2019) 571–580.

[37] L. Xu, Q. Jiang, Z. Xiao, X. Li, J. Huo, S. Wang, L. Dai, Plasma-engraved Co_3O_4 nanosheets with oxygen vacancies and high surface area for the oxygen evolution reaction, Angew. Chem. Int. Ed. 128 (2016) 5363–5367.

[38] J. Bao, X. Zhang, B. Fan, J. Zhang, M. Zhou, W. Yang, X. Hu, H. Wang, B. Pan, Y. Xie, Ultrathin spinel-structured nanosheets rich in oxygen deficiencies for enhanced electrocatalytic water oxidation, Angew. Chem. Int. Ed. 54 (2015) 7399–7404.

[39] Y. Dai, J. Gu, S. Tian, Y. Wu, J. Chen, F. Li, Y. Du, L. Peng, W. Ding, Y. Yang, γ-Al_2O_3 sheet-stabilized isolate Co^{2+} for catalytic propane dehydrogenation, J. Catal. 381 (2020) 482–492.

[40] N.K. Nagpal, Water Uuality Guidelines for Cobalt, Government of British Columbia, (2004).

[41] J.E. Yang, M. Zhu, X. Duan, S. Wang, B. Yuan, M. Fu, The mechanistic difference of ^{1}T–^{2}H MoS_2 homojunctions in persulfates activation: structure-dependent oxidation pathways, Appl. Catal. B Environ. (2021) 120460.

[42] Q. Pan, Q. Gao, G. Gao, M. Liu, B. Han, K. Xia, C. Zhou, Composition-engineered $LaCoO_3$-based monolithic catalysts for easily operational and robust peroxymonosulfate activation, Chem. Eng. J. 424 (2021), 130574.

[43] H. Gao, C. Huang, L. Mao, B. Shao, J. Shao, Z. Yan, M. Tang, B. Zhu, First direct and unequivocal electron spin resonance spin-trapping evidence for ph-dependent production of hydroxyl radicals from sulfate radicals, Environ. Sci. Technol. 54 (2020) 14046–14056.

[44] M. Zhu, D. Guan, Z. Hu, H. Lin, C. Chen, H. Sheu, S. Wang, J. Zhou, W. Zhou, Z. Shao, Synergistic effects in ordered Co oxides for boosting catalytic activity in advanced oxidation processes, Appl. Catal. B Environ. 297 (2021) 120463.

[45] C. Liu, J. Qian, Y. Ye, H. Zhou, C. Sun, C. Sheehan, Z. Zhang, G. Wan, Y. Liu, J. Guo, S. Li, H. Shin, S. Hwang, T.B. Gunnoe, W.A. Goddard, S. Zhang, Oxygen evolution reaction over catalytic single-site Co in a well-defined brookite TiO_2 nanorod surface, Nat. Catal. 4 (2021) 36–45.

[46] Y. Ye, M. Kapilashrami, C. Chuang, Y. Liu, P. Glans, J. Guo, X-ray spectroscopies studies of the 3d transition metal oxides and applications of photocatalysis, Mrs Commun. 7 (2017) 53–66.

[47] C.X. Kronawitter, J.R. Bakke, D.A. Wheeler, W. Wang, C. Chang, B.R. Antoun, J. Z. Zhang, J. Guo, S.F. Bent, S.S. Mao, L. Vayssieres, Electron enrichment in 3d transition metal oxide hetero-nanostructures, Nano Lett. 11 (2011) 3855–3861.

[48] A.M. Hibberd, H.Q. Doan, E.N. Glass, F.M.F. de Groot, C.L. Hill, T. Cuk, Co polyoxometalates and a Co_3O_4 thin film investigated by L-edge X-ray absorption spectroscopy, J. Phys. Chem. C 119 (2015) 4173–4179.

[49] D. Guan, J. Zhou, Z. Hu, W. Zhou, X. Xu, Y. Zhong, B. Liu, Y. Chen, M. Xu, H.J. Lin, C.T. Chen, J.Q. Wang, Z. Shao, Searching general sufficient-and-necessary conditions for ultrafast hydrogen-evolving electrocatalysis, Adv. Funct. Mater. 29 (2019) 1900704.

[50] C.F. Chang, Z. Hu, H. Wu, T. Burnus, N. Hollmann, M. Benomar, T. Lorenz, A. Tanaka, H.J. Lin, H.H. Hsieh, C.T. Chen, L.H. Tjeng, Spin blockade, orbital occupation, and charge ordering in $La_{1.5}Sr_{0.5}CoO_4$, Phys. Rev. Lett. 102 (2009).

[51] J. Cao, S. Sun, X. Li, Z. Yang, W. Xiong, Y. Wu, M. Jia, Y. Zhou, C. Zhou, Y. Zhang, Efficient charge transfer in aluminum-cobalt layered double hydroxide derived from Co-ZIF for enhanced catalytic degradation of tetracycline through peroxymonosulfate activation, Chem. Eng. J. 382 (2020), 122802.